Journal of Materials Chemistry A

ROYAL SOCIETY OF CHEMISTRY

PAPER

View Article Online
View Journal

Cite this: DOI: 10.1039/d4ta05014b

Ferroelectricity-enhanced potassium-ion storage in van der Waals layered $CuInP_2S_6$†

Po-Wen Chien,‡ Yu-Bo Hung,‡ Yi-Chun Yang and Hsing-Yu Tuan *

We integrate ferroelectric principles into two-dimensional (2D) van der Waals materials to enhance both charge and potassium ion (K^+) transport at the electrode interface. $CuInP_2S_6$ (CIPS) has a distinct room-temperature ferroelectric field effect due to the unique ordering of Cu and In ions in the CIPS lattice, which disrupts its centrosymmetry and causes significant spontaneous polarization. Its natural dipole moment creates a persistent polarizing electric field, facilitating fast carrier transfer from the material's bulk to its surface, boosting ionic conductivity under high electric fields. Utilizing the synergistic effects, layered CIPS coupled with graphene (CIPS@G) exhibits high specific capacity, superior long cycling stability and outstanding rate performance. The CIPS@G composite in a potassium-ion battery (PIB) offers a reversible capacity of 565 mA h g^{-1} at 50 mA g^{-1}, robust stability over 1000 cycles, and high rate performance (10 A g^{-1}), and a cycle life exceeding 400 cycles was also achieved when assembled in a full battery. In hybrid capacitors, CIPS@G stands out with superior rate performance up to 2.0 A g^{-1} and high energy density (40 W h kg^{-1}) at 2.0 A g^{-1}, surpassing other PIB phosphide and sulfide anodes reported to date. These results show that high-rate nanochannels between 2D CIPS nanosheets and graphene, paired with CIPS's ferroelectric polarization, improve electronic conductivity, support K^+ diffusion, relieve CIPS aggregation, and buffer volume changes. The study on enhancing K^+ performance in 2D materials through the integration of ferroelectric field principles holds promise for pioneering advancements in electrochemical systems.

Received 19th July 2024
Accepted 22nd September 2024

DOI: 10.1039/d4ta05014b

rsc.li/materials-a

1 Introduction

Potassium-ion batteries (PIBs), next-generation energy storage systems, are low-cost alternatives to lithium-ion batteries (LIBs).[1] With 1.5 wt% potassium *versus* 0.0017 wt% lithium, and considering potassium's weak Lewis acidity and its similarity to lithium in ionic conductivity, mobility, Stokes radius, and cell voltage (−2.93 V *vs.* SHE compared to lithium's −3.04 V *vs.* SHE) in carbonate solvents, PIBs have significant competitive advantages compared to LIBs.[2–6] PIBs are seen as potential candidates for large-scale energy storage systems. Despite sharing working principles with LIBs, many electrode materials designed for LIBs are not suitable for PIBs due to the larger ionic radius of K^+ (1.38 Å compared to lithium's 0.76 Å).[7] Most PIB anode materials encounter issues like slow ion diffusion, significant volume change, low capacity, and poor cycle stability, causing irreversible electrode degradation and subpar dynamic response and rate performance.[8,9] Carbon materials, like graphite, often show disappointing capacity (only 279 mA h g^{-1} theoretically),[10] and their ordered lattice and narrow interlayer spacing severely restrict the diffusion of K^+, leading to incomplete intercalation at high current densities and drastic capacity loss at low temperatures.[11] These problems worsen at the high current densities and large areal capacities required by next-generation batteries. Hence, finding advanced anode materials to overcome these challenges is essential for the practical use of PIBs.

Owing to their distinct structure, modifiable composition, and pronounced surface reactivity, layered transition metal thiophosphates, $M_2P_2Ch_6$ (M = metal; Ch = S, Se), are anticipated to be energy storage materials.[12,13] The layered metal chalcophosphate family consists of two-dimensional (2D) semiconductor plates held together through weak van der Waals (vdW) forces, containing ethane-like $[P_2S_6]^{4-}$ or $[P_2Se_6]^{4-}$ bicones, counterpoised by a honeycomb arrangement of octahedrally coordinated cations.[14] The $[P_2S_6]^{4-}$ or $[P_2Se_6]^{4-}$ polyanions' flexibility allows octahedral cationic sites to accommodate +1, +2, +3, and +4 metals with an average formal charge of +2, facilitating tunable properties like the bandgap and magnetism within the semiconductor region.[15] Such tunability makes $M_2P_2Ch_6$ and other 2D materials promising for innovative research. For instance, Wu *et al.* introduced a unique bimetallic thiophosphate alloy $Zn_xCo_{1-x}PS_3$ and CoS_2 as a 2D/3D heterostructure of $Zn_xCo_{1-x}PS_3/CoS_2$. The alloyed Zn

Department of Chemical Engineering, National Tsing Hua University, Hsinchu 30013, Taiwan. E-mail: hytuan@che.nthu.edu.tw

† Electronic supplementary information (ESI) available. See DOI: https://doi.org/10.1039/d4ta05014b

‡ These authors contributed equally to this work and share first authorship.

atoms tend to substitute Co atoms in $CoPS_3$ on various sides (termed ZCPS-Y), adjusting the electronic structure and creating an asymmetric electric field, thereby enhancing lithium storage performance.[16] Yet, the bulk $M_2P_2Ch_6$ compounds used for PIBs show minimal specific capacity and cyclability. The use of $M_2P_2Ch_6$ in PIBs has drawbacks. For example, van der Waals forces lead to the stacking of adjacent 2D nanosheets, reducing surface area, limiting ion diffusion, and impeding rapid electron and ion transport, which ultimately degrades electrochemical performance.[17,18]

2D ferroelectric materials demonstrate remarkable polarization coupled with distinguished electronic characteristics. Additionally, their inherent stable, layered configuration and pristine surfaces render them particularly suitable for comprehensive studies of ferroelectricity in atomic layer confinement.[19] $M_2P_2Ch_6$ have various unique properties. Particularly notable is $CuInP_2S_6$ (CIPS), which exhibits room-temperature ferroelectricity even when extremely thin. The ferroelectric nature of CIPS, a 2D ferroelectric material, originates from the off-center ordering of Cu ion sites along the *z*-direction. Additionally, the displacement of In ions within each layer in the opposite direction further contributes to this property. Such disruptions in CIPS's symmetry result in multiple spontaneous polarizations.[20] Further studies show that CIPS's Cu ions can be dislocated from the lattice, forming switchable electric dipoles as they traverse the lattice. CIPS's inherent spontaneous dipole moment can create a permanent polarizing electric field, serving as a direct force for the efficient spatial separation and rapid transfer of carriers from the bulk to the surface, facilitating high ionic conductivity even under elevated electric fields. Moreover, due to the weak van der Waals gaps present in 2D materials, CIPS can be readily exfoliated from the bulk crystals and interfaced with other 2D materials in an electric field tunable manner.[21,22] Recently, Liu *et al.* have utilized CIPS nanosheets and g-C_3N_4 ultrathin sheets to build 2D/2D heterostructures. The interaction of the heterostructure and the ferroelectric polarization field effectively enhanced photogenerated charge separation and transfer, thus improving photocatalytic H_2 performance.[23]

In this study, we show that CIPS nanosheets exhibit a unique room-temperature ferroelectric field effect, enabling efficient K^+ transport at the electrode interface due to their significant polarization and exceptional electronic properties. Their innate dipole moment produces a permanent electric field, driving rapid carrier transfer from the material's bulk to its surface, enhancing ionic conductivity in high electric fields. Through systematic experimentation, we observed that the composite of CIPS integrated with graphene (denoted as CIPS@G) exhibits salient characteristics: it possesses significant capacity, exemplifies enhanced long-term cycling stability, and showcases exceptional rate capability.[24,25] When assembled into the PIB system, the CIPS@G composite shows a noteworthy reversible capacity of 565 mA h g^{-1} at 50 mA g^{-1}. Furthermore, it shows consistent cycling performance even after undergoing 1000 cycles at 0.5 A g^{-1}, along with robust performance at rates as high as 10 A g^{-1}. We also constructed full cells and hybrid capacitors, highlighting their practical application potential. The synergy between the high-speed charge channels in 2D CIPS nanosheets, 2D graphene, and the ferroelectric field of CIPS enhances conductivity, improves K^+ movement, and reduces CIPS aggregation and volume shifts. The unique design concept of this work, with both the ferroelectric effect and two-dimensional materials, expands its application as a high-performance PIB advanced anode.

2 Experimental section

Materials

Copper particles with a size under 425 microns and 99.5% purity, 97% pure red phosphorus powder, 98% pure chunks of potassium metal in mineral oil, 99.5% pure potassium hexacyanoferrate(II) trihydrate, 99% anhydrous dimethyl carbonate (DMC), and sodium carboxymethyl cellulose with an average molecular weight of around 700 000 were all obtained from Sigma-Aldrich. Sulfur powder with a purity greater than 99% was sourced from Alfa-Aesar. Potassium bis(fluorosulfonyl) imide (KFSI) with 97% purity was purchased from Combi-Blocks. Coin-type cells (CR2032) and Super-P were procured from Shining Energy. Glass fiber was acquired from Advantec. Copper foil came from the Chang-Chun Group.

CIPS synthesis

CIPS was synthesized through a conventional solid-state reaction process, using powders of nominal composition with a total weight of 200 mg. The powders were loaded into quartz tubes and sealed under a dynamic vacuum pressure of 3.5×10^{-2} Pa. Next, these sealed samples underwent a controlled heating process in a muffle furnace, commencing at room temperature and gradually increasing up to 750 °C at a 1 °C min^{-1}. After maintaining this temperature for 48 hours, the furnace was left to naturally cool back to room temperature. Subsequently, a set of samples was collected.

$FePS_3$ synthesis

$FePS_3$ was synthesized through a conventional solid-state reaction process, using powders of nominal composition with a total weight of 200 mg. The powders were loaded into quartz tubes and sealed under a dynamic vacuum pressure of 3.5×10^{-2} Pa. Next, these sealed samples underwent a controlled heating process in a muffle furnace, commencing at room temperature and gradually increasing up to 750 °C at a 1 °C min^{-1}. After maintaining this temperature for 48 hours, the furnace was left to naturally cool back to room temperature. Subsequently, a set of samples was collected.

Synthesis of CIPS@G and $FePS_3$@G composites

Both composites were fabricated using high-energy mechanical milling (HEMM). The mixture of CIPS and graphene with a mass ratio of 3 : 1 was sealed in a stainless-steel grinding jar with stainless steel balls, all of which are within an argon-filled glovebox. The ball-to-powder mass ratio was roughly 180 : 1. This blend was then subjected to ball milling for a 24 hour period.

Prussian blue (PB) synthesis

In the standard protocol, Solution A was prepared by dissolving 5 mmol of $FeCl_2 \cdot 4H_2O$ in 100 ml of deionized (DI) water. Simultaneously, Solution B was created by dissolving 5 mmol of $K_4Fe(CN)_6 \cdot 3H_2O$, 10 mmol of potassium citrate, and an excess of potassium chloride in DI water. Solution A was gradually added to solution B using the precipitation method, followed by a 6 hour settling period. The resultant material was subjected to centrifugation, underwent three times of washing with DI water, and was subsequently dried at 80 °C in a CVD system for two hours.

Materials characterization

The sample morphology was examined using a Hitachi SU8010 SEM fitted with an energy-dispersive X-ray spectroscopy (EDS) detector. A JEOL JEM-ARM200FTH TEM, with services provided by NTHU and an accelerating voltage of 200 kV, was used for detailed structural analysis. X-ray diffraction using a Bruker D8 ADVANCE with Cu-Kα radiation ($\lambda = 1.54$ Å) was performed for structural and compositional analysis. Oxidation states were identified through high-resolution X-ray photoelectron spectroscopy (XPS, ULVAC-PH, PHI Quantera II, NTHU). Raman spectroscopy was conducted using a Micro Raman Identify Dual (MRID), and atomic force microscopy (AFM) was done using a Bruker Dimension Icon.

Electrochemical measurements

A homogeneous slurry, made from 70% CIPS@G, 20% Super-P carbon black, and 10% NaCMC in DI water, was coated on Cu foil and dried at 80 °C for one hour. The mass loading of the active material ranged between 0.7 and 1.0 mg cm^{-2}. The half cells were constructed using potassium foil as the counter electrode, 1 M KFSI in DMC as the electrolyte, and glass fiber filters from Advantec as separators. CR2032 coin cells were assembled inside an argon-filled glovebox, where moisture and oxygen levels were maintained below 1 ppm. Charge/discharge cycles were examined using a NEWARE CT-4000 battery measurement system within a 0.01–3.0 V *vs.* K^+/K range. The GITT was performed using a Maccor Series 4000 battery test system. CV and EIS were conducted on a Bio-Logic-Science Instruments VMP3 workstation.

Computational details

Spin-polarized Density Functional Theory (DFT) calculations were executed using the Vienna *ab initio* Simulation Package (VASP). The projector-augmented wave (PAW) approach, along with the Perdew–Burke–Ernzerhof (PBE) exchange–correlation functional, was used for modeling valence electron–core interactions. We employed a plane wave basis with a kinetic energy cutoff of 450 eV. All considered structures were optimized until both the energy and residual force reached convergence thresholds of 10^{-5} eV and 0.03 eV $Å^{-1}$, respectively. To accurately determine adsorption strength, the DFT-D3 method was applied. A 20 Å vacuum layer was included, and a $1 \times 1 \times 1$ Monkhorst–Pack grid was sampled. The pathways for K^+ migration, along with the associated energy barriers, were refined using the climbing image nudged elastic band technique.

Assembly of the full cell (CIPS@G//PB)

The overall cathode-to-anode surface charge ratio was held constant at 1. Both the anode and cathode underwent a 23-cycle preactivation procedure, which involved discharging to 2 V and 0.01 V, followed by a constant voltage process to stabilize the electrodes. 1 M KFSI in DMC electrolyte solution was used, and the working voltage window was established between 1 V and 3.8 V.

Assembly of the PIHC (CIPS@G//AC)

The hybrid capacitor featured CIPS@G as the anode and active carbon as the cathode, with an overall mass ratio of 1. Before the capacitor was assembled, the anode went through a 23-cycle preactivation process, culminating in a discharge to 0.01 V. The electrolyte used was 1 M KFSI in DMC, and the operational voltage window of the device was defined between 0.01 V and 3.8 V.

3 Results and discussion

CIPS was prepared *via* a solid-state reaction.[26] High-purity elements of copper (Cu), indium (In), phosphorus (P), and sulfur (S) were sealed at a 1 : 1 : 2 : 6 molar ratio in a vacuum quartz tube and then heated to 750 °C in a high-temperature furnace at a 1 °C per minute rate and held for 48 hours, producing layered CIPS crystals (Fig. S1, ESI†).[27] CIPS was analyzed using powder X-ray diffraction (PXRD). Fig. 1a shows primary diffraction peaks at 14°, 28°, 30°, 35°, 42°, 48°, 52°, 57°, and 64°, corresponding to the (002), (004), (130), (041), (222), (−314), (060), (008), and (400) planes of CIPS (JCPDS no. 04-012-9227), confirming CIPS as a pure monoclinic structure. The crystallographic parameters of $CuInP_2S_6$ refined by the Rietveld method have been added to Table S1 (ESI†). The hexagonal ABC sulfur-stacked CIPS crystal structure, interspersed with Cu, In, and P–P pairs and vdW gaps, is shown in Fig. 1b.[28] Through scanning electron microscopy (SEM) and transmission electron microscopy (TEM), varying degrees of stacking and layered structures of CIPS nanosheets were observed. Fig. 1c illustrates the stacking of CIPS at a scale of 2 μm, while Fig. 1d shows minimal stacking of CIPS (horizontal dimension approximately 500 nm). Fig. 1e displays the thickness of individual CIPS nanosheets measured by atomic force microscopy (AFM), which is approximately 40 nm. These nanosheets are uniformly dispersed on the substrate within the thickness range of 36–40 nm (as shown in Fig. 1f). The elemental distribution maps (TEM-EDS) exhibit the uniform distribution of Cu, In, P, and S on the nanosheets, ruling out the possibility of phase separation (Fig. 1g–k).[29] The quantitative results of EDS mapping are presented in Fig. S2 (ESI†). To further verify the elemental composition of CIPS, analysis was performed using inductively coupled plasma atomic emission spectroscopy (ICP). The ICP results indicate that the atomic ratio of Cu, In, P, and S is close

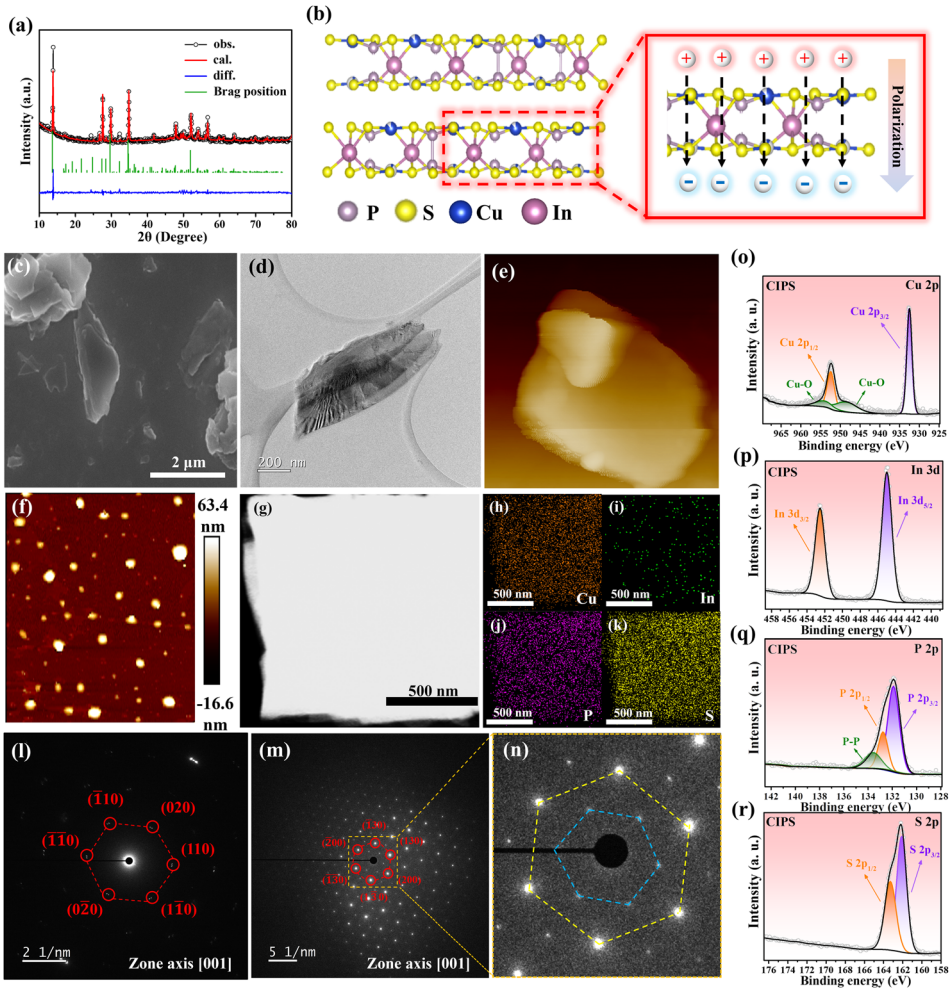

Fig. 1 (a) XRD pattern of CIPS nanoflakes. (b) Crystal structure of CIPS nanoflakes. (c) SEM image, (d) TEM image and (e and f) AFM topography images of a CIPS nanosheet, and (g–k) EDS mapping images of CIPS, along with the corresponding elements of Cu, In, P and S. (l–n) SAED patterns of CIPS along the [001] axis. (o–r) High-resolution Cu 2p, In 3d, P 2p, and S 2p XPS spectra.

to 1 : 1 : 2 : 6 (Table S2†).[30] In Fig. 1l–n, selected-area electron diffraction (SAED) patterns were obtained from the [001] axis orientation. At a scale of 2 nm^{-1}, hexagonal facets consisting of atomic planes with Miller indices $(\bar{1}10)$, (020), (110), $(1\bar{1}0)$, $(0\bar{2}0)$, and $(\bar{1}\bar{1}0)$ were observed. At a scale of 5 nm^{-1}, additional hexagonal facets composed of atomic planes with Miller indices $(\bar{1}30)$, (130), (200), $(1\bar{3}0)$, $(\bar{2}00)$, and $(\bar{1}\bar{3}0)$ were observed. The SAED patterns reveal distinct diffraction spots and rotationally symmetric hexagonal structures, indicating the high crystallinity of the CIPS sample, which is consistent with the results obtained fromPXRD. As shown in Fig. S3 (ESI†), high-resolution X-ray photoelectron spectroscopy (XPS) analysis was conducted. The Cu^{+} peaks appear at 951.8 eV ($2p_{1/2}$) and 932.7 eV ($2p_{3/2}$) in the Cu 2p spectra. Additionally, peaks at 948.7 eV and 954.2 eV are attributed to the oxidation states of copper (Fig. 1o).[31,32] In the In 3d XPS spectra, the peak positions of In 3d are observed at 452.5 eV and 445 eV, corresponding to $3d_{3/2}$ and $3d_{5/2}$, respectively (Fig. 1p). The peaks in the P 2p spectra can be attributed to 132.6 eV ($2p_{1/2}$) and 131.8 eV ($2p_{3/2}$). The peak at 133.29 eV is attributed to the P–P bond (Fig. 1q),[33] while the peaks at 162.1 eV ($2p_{1/2}$) and 163.3 eV ($2p_{3/2}$) are attributed to S^{2-} in the P_2S_6 units (Fig. 1r).[34] Overall, these findings confirm the high-quality and phase-pure structure of the CIPS crystals.

To confirm layered CIPS's ferroelectricity, temperature-dependent piezoresponse force microscopy (PFM) was conducted.[35] Fig. 2 displays the PFM magnitude and phase images at 25 °C and 50 °C. It is important to highlight that the ferroelectric properties of CIPS vanish when the temperature exceeds 40 °C.[28] Additionally, the potassium metal in the electrode would melt beyond 60 °C. Due to these considerations, we selected 50 °C as the temperature for comparing the ferroelectric properties. The PFM magnitude indicates the piezoelectric response linked to remanent polarization (Pr), and the phase reveals the polarization direction in each domain. Vertical PFM measurements reveal clear out-of-plane polarization in the CIPS nanosheet, evident from the PFM magnitude (Fig. 2a) and domain structure (Fig. 2d), confirming robust ferroelectricity. However, above the Curie temperature (T_c), the PFM amplitude and magnetic domain clarity diminish (Fig. 2b and e), corresponding to the transition to a nonpolar paraelectric phase.

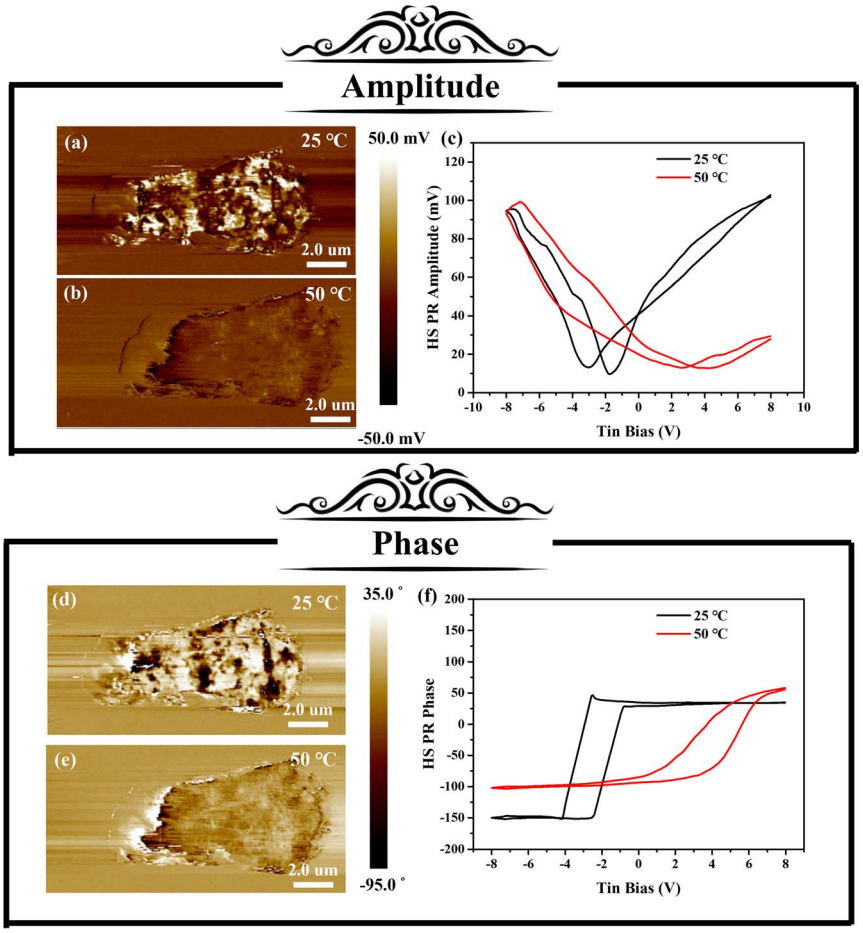

Fig. 2 The PFM amplitude images of a CIPS nanosheet at (a) 25 °C and (b) 50 °C. (c) Temperature-dependent DART-PFM amplitude hysteresis loop at different temperatures. The corresponding PFM images of the CIPS nanosheet at (d) 25 °C and (e) 50 °C. (f) Temperature-dependent DART-PFM phase hysteresis loop at different temperatures.

Fig. 2c presents the DART-PFM phase hysteresis loops of the CIPS nanosheet at 25 °C and 50 °C. At room temperature, a distinct ferroelectric PFM hysteresis loop with evident polarization switching is seen, but at 50 °C, there is no noticeable phase change.[36–38]

To integrate CIPS into PIB, we engineered a CIPS@G composite with a graphene coating, minimizing volume expansion in CIPS during potassiation and de-potassiation, thus stabilizing coulombic efficiency across extended cycles.[39–41] The CIPS@G anode's performance in a PIB was analyzed in a half-cell arrangement. After mixing with graphene, the XRD pattern of CIPS@G shows the same diffraction peak position in Fig. S4 (ESI†) compared with the raw material. Then, CIPS@G is uniformly encapsulated in graphite with a flake structure (Fig. S5, ESI†), while the presence of graphene was confirmed by XPS analysis and Raman spectroscopy (Fig. S6–S8, ESI†). Additionally, the cycling performance of CIPS was shown (Fig. S9, ESI†). Cyclic voltammetry (CV) measurements (0.1 mV s^{-1}, 0.01–3.0 V *vs.* K/K^+) detailed the reaction behavior of the CIPS@G electrode (see Fig. 3a), where the capacity efficiency is reflected by the utilization of conversion products like K_2S_4, K_2S_3, and K_4P_3. On the CV curve, the initial cathodic peak at 1.0 V vanishes in later cycles due to the irreversible reaction of CIPS@G with K^+ and solid electrolyte interface (SEI) formation from KFSI decomposition.[42] We observed a sharp cathodic peak at 0.02 V, and a similar phenomenon was reported by Peng *et al.* in the CV curve of Cu_2S@NC for PIB, where a sharp cathodic peak also appeared at 0.02 V.[43] Therefore, this peak is contributed by the insertion of K^+ into the carbon layer.[44] Later cycles display overlapping curves between 0.5 V and 1.0 V, hinting at multi-step reactions, potentially forming K_2S_4 and K_2S_3 from CIPS@G.[45] The anodic sweep reveals a peak at 0.3 V, from carbon deintercalation,[46] and two oxidation peaks near 0.9 V and 2.4 V, corresponding to the transformations of P and S, respectively. Fig. S10 (ESI†) displays the CIPS@G electrode's galvanostatic charge–discharge (GCD) curves, consistent with CV analysis, at 50 mA g^{-1} within a 0.01–3.00 V range. The initial discharge capacity was 774 mA h g^{-1}, and the initial coulombic efficiency (ICE) was 75.1%, with irreversible capacity loss due to SEI layer formation. After the first cycle, GCD curves in the subsequent cycles overlapped, consistent with CV curve results.[47] Moreover, the impact of ferroelectricity properties on electrochemical performance was further observed through the introduction of $FePS_3$. Fig. S11 and S12 (ESI†) show the XRD pattern of $FePS_3$, and $FePS_3$@G crystals consist of stacked single-layer assemblies, indicating that CIPS and $FePS_3$ have similar structures. CIPS@G

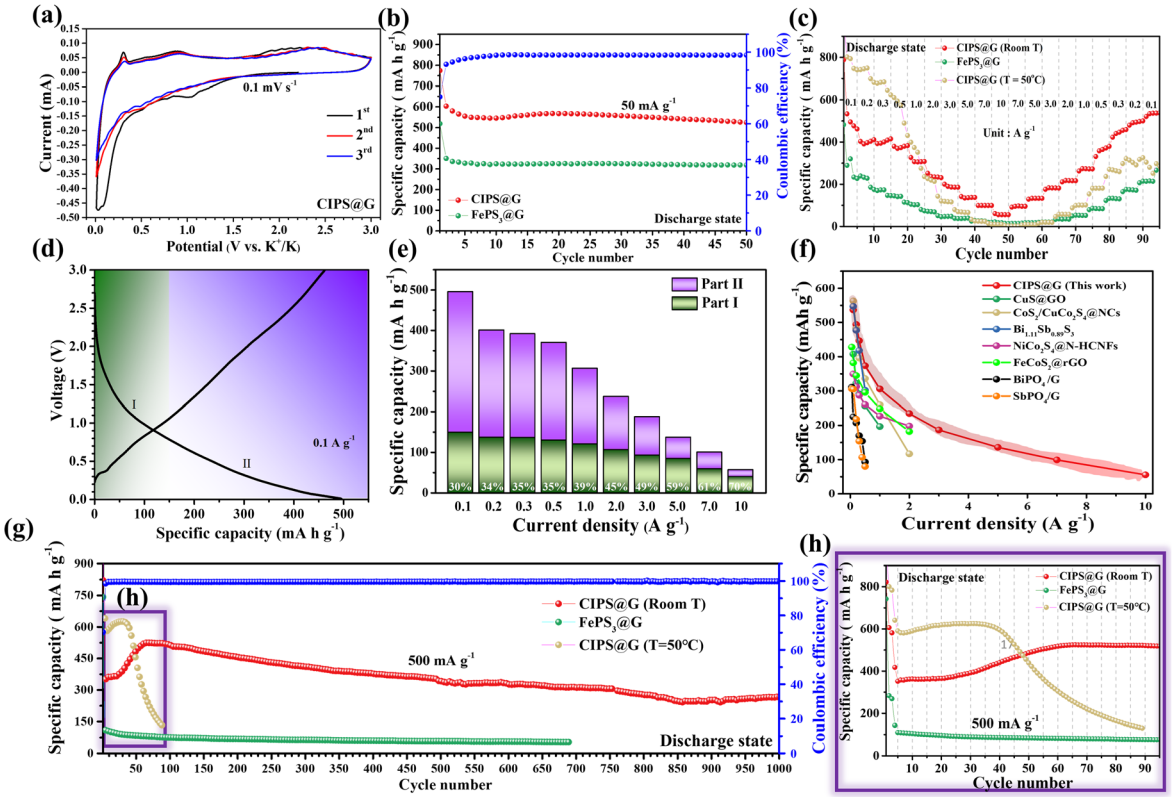

Fig. 3 (a) CV curves of CIPS@G at 0.1 mV s^{-1}. (b) Cycling performance at 50 mA g^{-1}. (c) Rate capability of CIPS@G at different temperatures and $FePS_3$@G from 0.1 A g^{-1} to 10 A g^{-1}. (d) GCD curves of CIPS@G at 0.1 A g^{-1}. (e) The bar chart of the calculated capacity contributions at different parts of the QV curves. (f) Comparison of rate performance between CIPS@G and other sulfide and phosphide-based anodes. (g) Long-term cycling performance of CIPS@G at 500 mA g^{-1}. (h) Cycling performance of the three electrodes before 100 cycles.

offers a reversible capacity of 565 mA h g^{-1} at 50 mA g^{-1}, whereas $FePS_3$@G only provides 324 mA h g^{-1}. Fig. 3b depicts the cycling stability of CIPS@G and $FePS_3$@G at 50 mA g^{-1}, highlighting the benefits of ferroelectricity. Furthermore, to elucidate the significance of ferroelectric effects, we detailed rate performance tests for CIPS@G and $FePS_3$@G at different temperatures, with current densities ranging from 0.1 to 10 A g^{-1}. Fig. 3c shows the superior performance of CIPS@G at room temperature across these densities, with capacities ranging from 534 mA h g^{-1} at 0.1 A g^{-1} to 56 mA h g^{-1} at 10 A g^{-1}. CIPS@G retains a capacity of 534 mA h g^{-1} when reverted to 0.1 A g^{-1}, indicating high stability. On the other hand, $FePS_3$@G has capacities ranging from 320 to 21 mA h g^{-1} across the mentioned current densities, suggesting that it struggles at high current densities. It should be noted that CIPS@G exhibits poor stability at 50 °C. Higher ambient temperatures provide favorable kinetic conditions for CIPS@G to exhibit higher capacity in the initial cycle, but in the subsequent cycles, the capacity declines continuously. This suggests that CIPS@G, which has lost its ferroelectric effect and no longer possesses excellent cycling performance.[48] Fig. 3d illustrates the GCD curves of the CIPS@G electrode at 0.1 A g^{-1}, while the GCD curves at rates ranging from 0.2 to 10 A g^{-1} are shown in Fig. S13 (ESI†). At high current densities, CIPS@G exhibits distinct plateaus and lower overpotentials, indicative of robust reaction kinetics and K^+ diffusion. The rate performance of charge–discharge curves is divided into two parts to assess the capacity of conversion reactions (Fig. 3e). The first part corresponds to the potassiation of CIPS in the first stage, while the second part encompasses the potassiation in the second and third stages. This confirms that the reversible capacity at high current densities mainly arises from the conversion reactions in the first part. The potassiation mechanism of CIPS will be elucidated in detail subsequently. Considering the abundant redox active sites in 2D materials coupled with the influence of ionic and ferroelectric fields, we assume that these factors enhance K^+ storage and intra-electrode migration. We compared the rate performance of CIPS@G with those of other sulfide and phosphide-based anodes by charting specific capacity *versus* current density (Fig. 3f). CIPS@G outperforms materials such as CuS@GO,[49] $CoS_2/CuCo_2S_4$@NCs,[50] $Bi_{1.11}Sb_{0.89}S_3$,[51] $NiCo_2S_4$@N-HCNFs,[52] $FeCoS_2$@rGO,[53] $BiPO_4$/G, and $SbPO_4$/G.[54] Fig. 3g shows the long-term test of the CIPS@G electrode at 500 mA g^{-1}. The CIPS@G electrode maintains a capacity of approximately 267 mA h g^{-1} after 1000 cycles at room temperature, with a coulombic efficiency of 99.9%. This efficiency is attributed to its surface treatment and consistent electrolyte contact. The observed increase in capacity during the initial 50 cycles may be attributed to stress-induced material fracturing during the phase transition process. The smaller fragments possess a larger surface area, facilitating reactions and the formation of a SEI

layer on the newly exposed fracture surfaces. As this process gradually stabilizes, CIPS@G exhibits excellent long-term cycling performance.[55] Additionally, CIPS@G gradually develops ion channels, consuming some electrolyte in the process. Once a certain number of cycles are completed, these ion channels stabilize, promoting more effective reactions with K^+ within the structure of CIPS@G.[56] In comparison, the $FePS_3$@G electrode exhibits poorer specific capacity at high current density. The limited specific capacity performance of $FePS_3$@G may be due to its lack of ferroelectric properties. As shown in Fig. 3h, despite the initially high capacity at 50 °C, a sharp decline is observed after approximately 50 cycles, attributed to the loss of ferroelectric field effects, leading to poor cycling stability thereafter. The outstanding electrochemical performance of CIPS@G at room temperature is attributed to its 2D structure and ferroelectric field. These features effectively address the volume changes induced by K^+ insertion and accelerate charge separation and transfer, thereby enhancing the battery's activity. It is important to note that in experiments conducted at various current densities, the initial discharge capacity corresponds to the reaction amount associated with the formation of the SEI layer. Therefore, the initial discharge capacity observed for CIPS@G is similar across different current densities.

The electrochemical process of K^+ storage in CIPS electrodes was examined by assessing the influence of structure evolution and interface on reversibility. A multi-technique approach comprising *ex situ* XRD, XPS, HRTEM, and SAED was employed to scrutinize potassium storage during the initial discharge/charge cycle.[57] Notably, the *ex situ* XRD analysis was performed over a 0.01 V to 3.00 V voltage range during these stages. Initially, at an open-circuit voltage (OCV) of approximately 2.2 V *versus* K^+/K, identifiable diffraction peaks corresponded to (002), (004), (130), (041), (222), (−314), (060), and (008) planes at specific angles. As the battery discharges to 1.5 V, the original diffraction peaks of CIPS gradually disappear, replaced by new peaks that emerge at 17.2°, 19.1°, 25.7°, 27.5°, 28.8°, 42.1°, and 43.4°. Some noise peaks are also observed, with the signal at 18° corresponding to K_2S_3 (PDF 04-007-0574), the signal at 22° corresponding to the residue of the electrolyte KFSI (PDF 04-020-3303), and the signals at 49° and 50° corresponding to $Cu_{0.9}In_{0.1}$ (PDF 04-004-5488) and $CuIn_{0.44}$ (PDF 04-004-8220), respectively. As these signals are relatively weak compared to the main characteristic peaks, they may represent the initiation of sulfur conversion and the onset of CuIn alloying, respectively. When the battery's voltage drops to 0.01 V, the diffraction peak associated with K_2S_4 recedes, and the KPS_3 phase vanishes. A new peak emerges at 28.1°, signifying the formation of K_2S_3 due to the completion of the sulfur conversion reaction. Meanwhile, the phosphorus in KPS_3 converts entirely to K_4P_3. In the subsequent charging cycle, the diffraction peaks of K_2S_4, K_2S_3, K_4P_3, and the CuIn alloy vanish, and CIPS peaks reappear, suggesting a reversible reaction. We employed *ex situ* HRTEM and SAED to analyze the morphology and crystallography of the CIPS anode under fully potassiated (D 0.01 V) and depotassiated (C 3.0 V) states. In the fully discharged state (0.01 V), calculated lattice spacings of 0.21, 0.215, 0.253, 0.281, 0.308, 0.32, and 0.326 nm were discerned in the HRTEM image. Spacings of 0.21, 0.215, and 0.253 nm matched the (1–34), (330), and (200) planes of the CuIn alloy, and 0.32 and 0.326 nm related to the (112) and (0–41) planes of K_2S_3 and K_2S_4. Spacings of 0.281 and 0.308 nm corresponded to the (114) and (130) planes of K_4P_3. Ring patterns associated with the CuIn alloy, K_2S_3, K_2S_4, and K_4P_3 were noted in the corresponding SAED, featuring the (112) plane of K_2S_3, the (130) plane of K_4P_3, and the (330) and (1–34) planes of the CuIn alloy, confirming the conversion reaction between CIPS and K^+. Post-charging to 3.0 V (C3.0 V, fully de-potassiated state), the CIPS (222) and (004) patterns reemerged, as observable in Fig. 3e. The associated diffraction ring's d-spacing coincided with CIPS, aligning with our *ex situ* XRD findings (Fig. 4a and b). After the first potassiation and de-potassiation, *ex situ* XPS was utilized to comprehend the role of each element in CIPS (Fig. 4g–j). Upon discharging to 0.01 V, the Cu 2p and In 3d spectra demonstrated that Cu^{1+} and In^{3+} reduced to Cu^0 (932.8 and 952.7 eV) and In^0 (443.6 and 451.3 eV) respectively, indicating a reduction of all multivalent cations in the CIPS lattice to M^0. Moreover, the existence of monovalent copper and trivalent indium at the fully de-potassiated state confirms the inference of the reversible conversion reaction (Fig. 4g and h). P 2p spectra (Fig. 5i) display a peak shift at 0.01 V towards lower binding energy due to K_4P_3 formation, while at 3.0 V, a shift towards higher binding energy indicates CIPS recombination. A similar observation is made in the S 2p spectra (Fig. 4j) with a peak shift at 0.01 V (K_2S_3 formation) and 3.0 V (CIPS recombination). In conclusion, the results from *ex situ* XRD, TEM, and XPS analyses inferred the CIPS reaction mechanism illustrated in Fig. 4k, along with the corresponding potassiation/de-potassiation conversion reaction equations as follows:[58]

Potassiation:

$$\text{Stage I: } CuInP_2S_6 + 2K^+ + 2e^- \rightarrow (CuIn)\text{alloy} + 2KPS_3$$

$$\text{Stage II: } 3KPS_3 + 7K^+ + 7e^- \rightarrow K_4P_3 + 3K_2S_4$$

$$\text{Stage III: } 3K_2S_4 + 2K^+ + 2e^- \rightarrow 4K_2S_3$$

Depotassiation:

$$\text{Stage IV: } 2K_4P_3 + 6K_2S_3 + 3(CuIn)\text{alloy} \rightarrow 3CuInP_2S_6 + 20K^+ + 20e^-$$

Through PFM analysis, we confirmed $FePS_3$'s antiferroelectric properties. Fig. 5a and b present the DART-PFM phase and amplitude hysteresis loops for CIPS@G and $FePS_3$@G, respectively. The reduced amplitude and absence of a significant phase shift in $FePS_3$@G, compared to CIPS@G, highlight its antiferroelectric nature. This inclusion of $FePS_3$@G is strategic for exploring how ferroelectric and antiferroelectric properties influence electrochemical performance. Importantly, to further understand the ferroelectric effect on K^+ storage, we monitored the ferroelectric properties of CIPS@G before and after 100 cycles using PFM. Fig. 5c and d demonstrate that

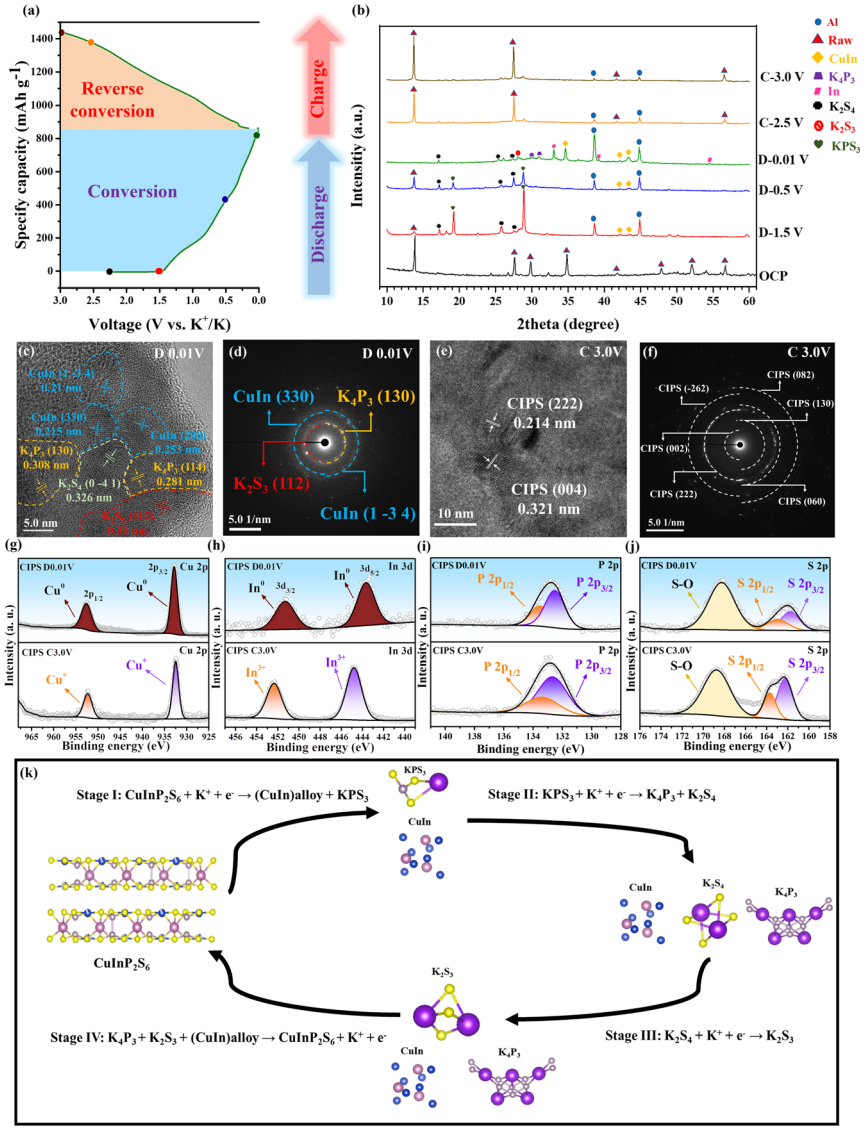

Fig. 4 (a) The initial charge and discharge profile of CIPS at 50 mA g^{-1}, as used in the *ex situ* XRD analyses presented in (b). *Ex situ* TEM and SAED patterns under potassiation conditions of (c and d) 0.01 V and depotassiation conditions of (e and f) 3.0 V. Comparison of the (g) Cu 2p, (h) In 3d, (i) P 2p, and (j) S 2p core-level spectra at the full potassiation state (0.01 V) and depotassiation state (3.0 V). (k) Schematic depiction of the reversible process of K^+ storage in the CIPS electrode during the charge and discharge cycles.

CIPS@G retains marked phase shifts and amplitudes post-cycling, evidencing the preservation of its ferroelectricity.

Considering the electrochemical behavior of CIPS at varying temperatures, it is inferred that the impressive performance of CIPS@G is likely linked to its ferroelectric properties. However, considering our proposed mechanism, which involves the alloying of CuIn and the formation of phosphorus potassium compounds and phosphorus sulfides during the potassiation process in CIPS, concerns arise regarding the continuity of the ferroelectric properties of CIPS throughout the electrochemical process. To address this, we conducted *ex situ* PFM measurements to monitor the ferroelectric properties of CIPS at various discharge potentials, as detailed in Fig. 5e–j. The experimental results show significant phase changes and amplitude variations at discharge potentials of 1 V, 0.5 V, and 0.01 V, confirming that CIPS retains its ferroelectric effect during cycling. This suggests that during the potassium intercalation process, the surface material participates actively in the reaction, primarily contributing to the capacitance, while the bulk of the material continues to provide a ferroelectric field throughout the cycle.

Fig. 6 provides a dynamic analysis of 2D ferroelectric CIPS@G and antiferroelectric $FePS_3$@G. CIPS@G shows excellent K^+ storage and cycling stability, which is related to its pseudocapacitive and diffusive behavior at different rates. To comprehend the high-rate performance and cycling stability brought about by ferroelectric properties, detailed kinetic analyses were conducted by recording the cyclic voltammograms (CVs) of CIPS@G and $FePS_3$@G anodes at varying scan rates (Fig. 6a and e). The CV curves, consistent in shape, show that the anodic peak potential gradually shifts to higher values as scan rates increase, an observation linked to the commonly

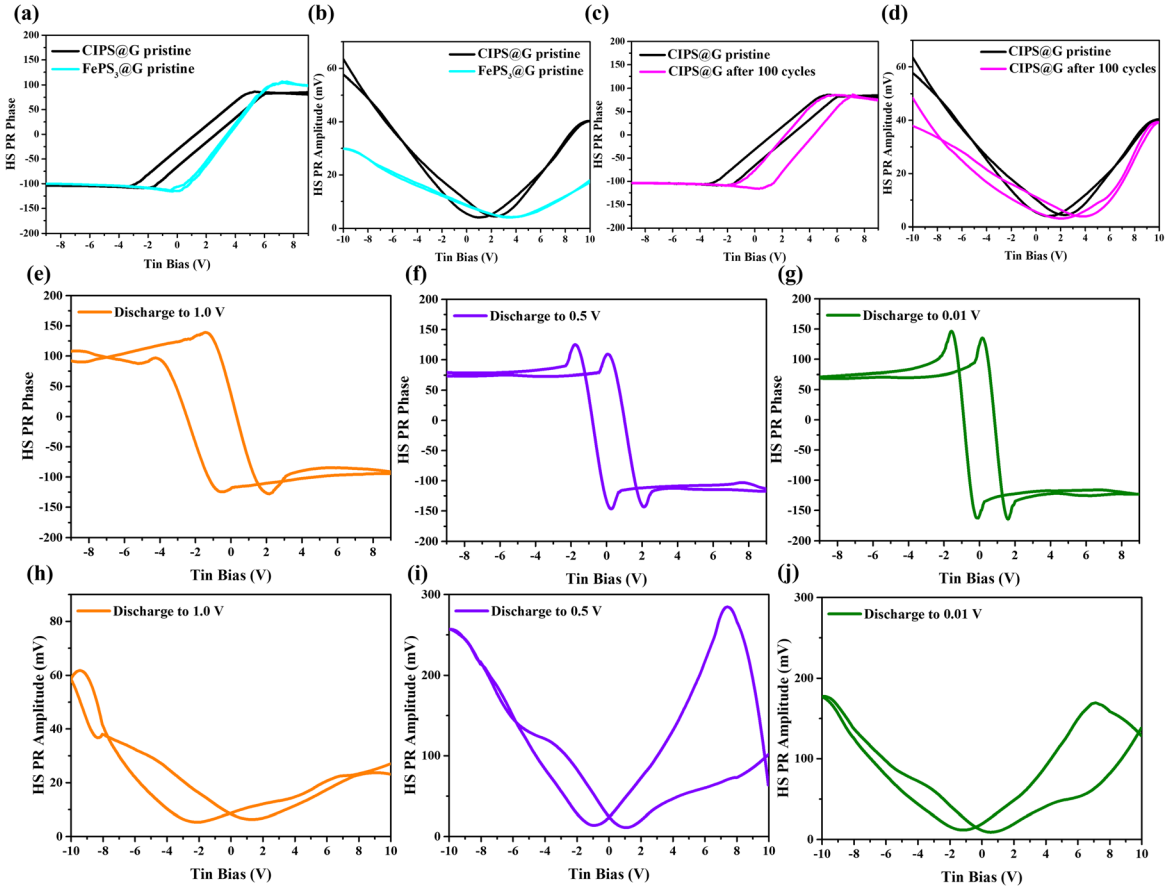

Fig. 5 (a) DART-PFM phase hysteresis loops and (b) amplitude hysteresis loops of pristine CIPS@G and $FePS_3$@G. The (c) DART-PFM phase hysteresis loops and (d) amplitude hysteresis loops of pristine CIPS@G and CIPS@G after 100 cycles. (e–g) Phase hysteresis loops of CIPS@G during the first discharge to 1 V, 0.5 V, and 0.01 V. (h–j) Amplitude hysteresis loops of CIPS@G during the first discharge to 1 V, 0.5 V, and 0.01 V.

reported electrode polarization process. The current (i) extracted from the CV curves and the scan rate (v) adhere to a power-law relationship, which considers both surface and diffusion dominated reactions, calculated using:[59,60]

$$i = av^b \quad (1)$$

$$\log i = b \times \log v + \log a \quad (2)$$

Here, a and b are tunable parameters within the power-law relationship. Notably, the b value is significant as it shows the kinetic contribution of the electrode surface from the linear fit slope of the logarithms of the peak current (i_p) and scan rate (v). Estimated from the slope of the $\log(i)$ *vs.* $\log(v)$ plot, the anodic and cathodic processes of CIPS@G revealed three main peaks with the respective b values of 0.73, 0.84, and 0.89 (Fig. 6b), and the b values corresponding to the three main peaks of $FePS_3$@G are 0.65, 0.63, and 0.74 (Fig. 6f). In general, when the b value is more than 0.75, the reaction is primarily capacitive; when it is less than 0.75, the reaction is diffusion-controlled.[61,62] Therefore, two of the aforementioned peaks of CIPS@G are defined as capacitive, implying a higher capacity contribution (%), relative to diffusion-controlled processes, at high current densities. The three peaks of anti-ferroelectric $FePS_3$@G exhibit diffusion-controlled behavior, possibly related to its anti-ferroelectric nature. Furthermore, we quantified the contributions of the capacitive effect and diffusion-controlled K^+ insertion by analyzing the CV curves at various scan rates, calculated *via*:

$$i = k_1 v^{\frac{1}{2}} + k_2 v \quad (3)$$

$$i/v^{\frac{1}{2}} = k_1 + k_2 v^{\frac{1}{2}} \quad (4)$$

In the given equations, $k_1 v^{\frac{1}{2}}$ symbolizes the diffusion-controlled (faradaic) portion, while $k_2 v$ indicates the pseudocapacitive-controlled (non-faradaic) part. By graphing $i(V)/v^{\frac{1}{2}}$ and $v^{\frac{1}{2}}$ within a certain potential range, the slope (k_2) and intercept (k_1) can be computed, quantifying the capacitive and diffusive contributions at a specific potential. Fig. 6c and g show that at a scan rate of 1.0 mV s^{-1}, the capacitive contributions of CIPS@G and $FePS_3$@G account for 62.22% and 40.53% of the total area, respectively. This indicates that the capacitive control of current on the inner surface of CIPS@G, attributed to its ferroelectric properties, is superior to diffusion-controlled current. Therefore, the high-rate performance of CIPS@G is better than that of ferroelectric $FePS_3$@G. The capacitive percentages of CIPS@G and $FePS_3$@G for scan rates from 0.2 to

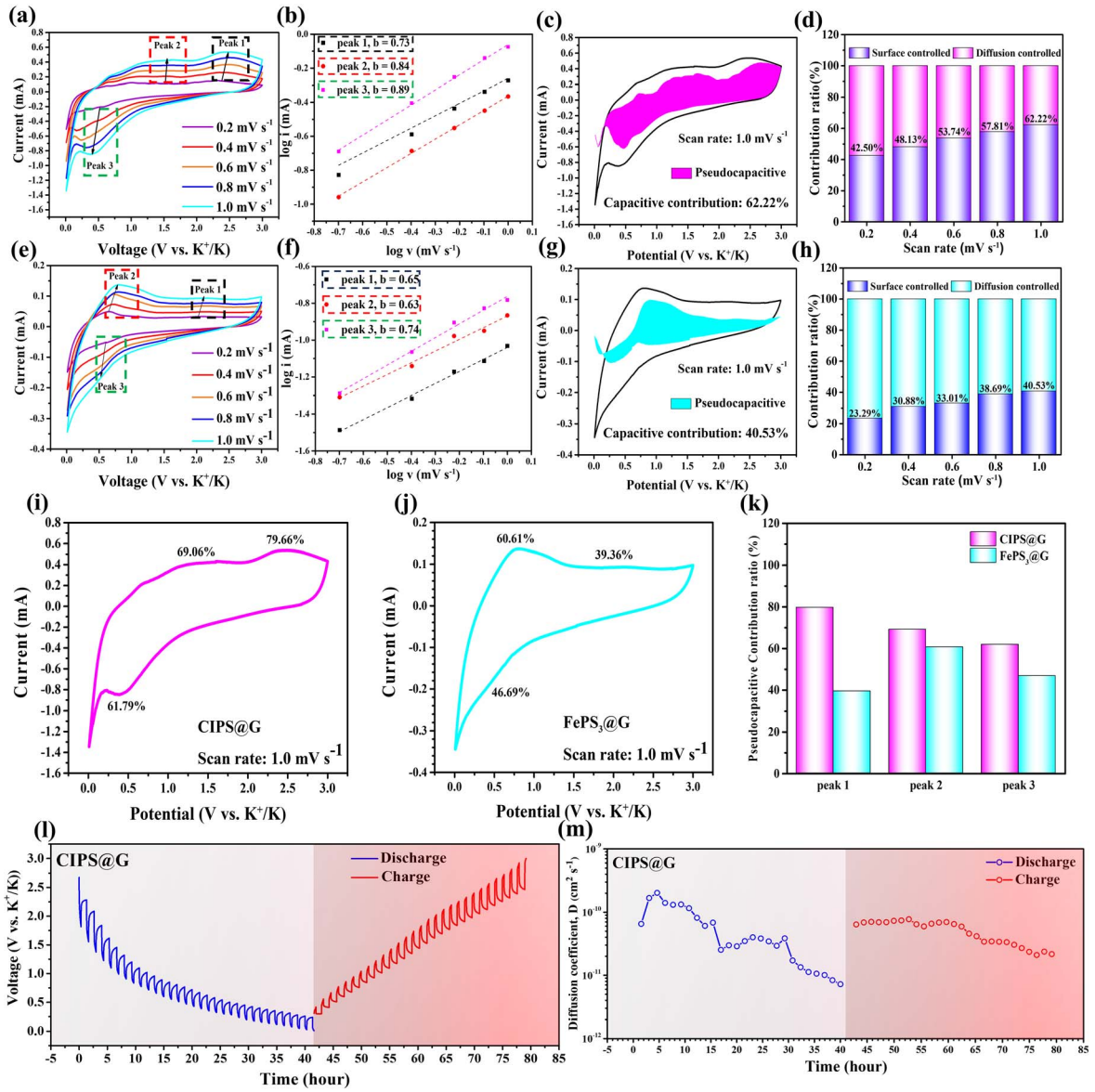

Fig. 6 (a) CV profile of the CIPS@G electrode at different scan rates. (b) Logarithm response current *versus* logarithm scan rate. (c) Pseudocapacitive contribution at a scan rate of 1.0 mV s^{-1}. (d) The ratio of pseudocapacitive and diffusion contributions at different scan rates, and (e) CV profile of the $FePS_3$@G electrode at different scan rates. (f) Logarithm response current *versus* logarithm scan rate. (g) Pseudocapacitive contribution at a scan rate of 1.0 mV s^{-1}. (h) The ratio of pseudocapacitive and diffusion contributions at different scan rates. (i) CIPS@G and (j) $FePS_3$@G pseudocapacitive contribution at a scan rate of 1.0 mV s^{-1} for peaks 1–3. (k) Comparison of pseudo-capacitance contributions for peaks 1–3 between CIPS@G and $FePS_3$@G. (l) GITT curves with a 20 min current pulse at 50 mA g^{-1} followed by a 1 hour relaxation period, and (m) the diffusion coefficients corresponding to each current pulse.

1.0 mV s^{-1} varied from 42.5% to 62.22%, and 23.29% to 40.53% (Fig. 6d and h). CIPS@G exhibits a higher pseudocapacitance ratio at different scan rates. This effect, likely due to the ferroelectric field facilitating electron and K^+ transport, enhances the material's rate capability and suggests efficient K^+ adsorption and fast reaction kinetics. To further confirm the effect of ferroelectric properties on the pseudocapacitive contribution, the CV curves of CIPS@G and $FePS_3$@G were recorded at a scan rate of 1.0 mV s^{-1}. Characteristic redox peak analysis was performed to determine the pseudocapacitive contribution proportion. According to eqn (3), the pseudocapacitive ($k_1 \times v$) and intercalation ($k_2 \times v^{1/2}$) contributions can be quantized.[63] For CIPS@G, the pseudocapacitive contribution of the peaks was 65.59%, 75.97%, and 73.24%, while $FePS_3$@G exhibited 41.92%, 56.55%, and 39.24% pseudocapacitive contributions. The pseudocapacitive contribution of $FePS_3$@G was lower than that of CIPS@G (Fig. 6i–k). This effect, likely due to the ferroelectric field facilitating electron and K^+ transport, enhances the material's rate capability and suggests efficient K^+ adsorption and fast reaction kinetics. To further explore the impact of the ferroelectric field, we used the galvanostatic intermittent titration technique (GITT) to analyze the diffusion coefficient of K^+

(D_{K^+}) during potassiation/de-potassiation (Fig. 6l). The D_{K^+} of CIPS@G was calculated using eqn (5) from GITT curves.[64,65]

$$D_{K^+} = \frac{4}{\pi\tau}L^2\left(\frac{\Delta E_s}{\Delta E_t}\right)^2 \quad (5)$$

In the equation, τ, ΔE_s, ΔE_t, and L denote the current pulse time, induced constant voltage change, potential change of the steady-state current pulse, and electrode thickness (Fig. S14 and S15, ESI†), respectively. Fig. 6l depicts the GITT curve of CIPS@G with a relaxation time of 1 hour and a pulse time of 20 minutes, while Fig. 6m illustrates the diffusion coefficients calculated during the discharge and charge processes.[66] The diffusion coefficients of CIPS@G exhibit a stable diffusion pattern, ranging from 10^{-9} to 10^{-12} cm^2 s^{-1}. In contrast, the diffusion coefficient of anti-ferroelectric $FePS_3$@G is approximately around 10^{-11} cm^2 s^{-1} (Fig. S16, ESI†). Table S3 (ESI†) summarizes the average diffusion coefficients of CIPS@G and $FePS_3$@G during the three potassium insertion stages. In the initial stage of potassium insertion, CIPS@G shows a higher diffusion coefficient due to its unique ferroelectric field, which likely accelerates the diffusion of ions and electrons during the charge/discharge processes, thereby enhancing the storage kinetics of K^+ during cycling. As the discharge depth increases, the slight decrease in the diffusion coefficient corresponds to the gradual transformation of CIPS@G during potassium insertion. However, $FePS_3$@G exhibits a stable diffusion coefficient across all three stages, which is overall slightly lower than that of CIPS@G. Due to the unique ferroelectric properties of CIPS@G, which significantly influence the diffusion coefficient during the potassium insertion process, this becomes one of the core reasons why CIPS@G is superior to $FePS_3$@G in potassium ion storage. Resistance measurements of CIPS@G were performed using electrochemical impedance spectroscopy (EIS). The Nyquist plots display a semicircle in the high-frequency region and a straight line in the low-frequency region, with the semicircle radius indicating K^+ diffusion impedance (Fig. S17, ESI†). The SEI, serving as an excellent ion-conductive membrane, plays a crucial role in diffusion impedance. Initially, CIPS@G exhibits a larger diffusion impedance due to the absence of an SEI film on the fresh electrode. When discharging to 0.5 V, the conductive CuIn alloy and gradually formed SEI layer reduce ion diffusion impedance. We speculate that the initial increase in impedance during de-potassiation is attributed to the initial presence of K_2S_3 and K_4P_3, as well as the carbon layer binding potassium ions, resulting in a larger diffusion impedance. Fig. S17b (ESI†) reveals a noticeable shift in the group resistance around 0.3 V. The low diffusion impedance caused by SEI formation during potassium insertion persists during de-potassiation. Therefore, it maintains a lower diffusion impedance in the subsequent charging process.

We performed Density Functional Theory (DFT) calculations to explore how the ferroelectric property influences the potassium-ion storage performance of the CIPS-based anode (Fig. 7 and S18–S21, ESI†). All simulations were conducted at 0 K. The material band gaps are depicted in Fig. 7a and b, with CIPS having a gap of 0.34 eV, while $FePS_3$ exhibits overlapping conduction and valence bands. The Density of States (DOS) for both CIPS and $FePS_3$ was studied to understand their electronic structures (Fig. 7c and d). The DOS of CIPS reveals that Cu and S primarily contribute to the valence band, while in the conduction band, the contributions follow the order S > P > Cu > In. In

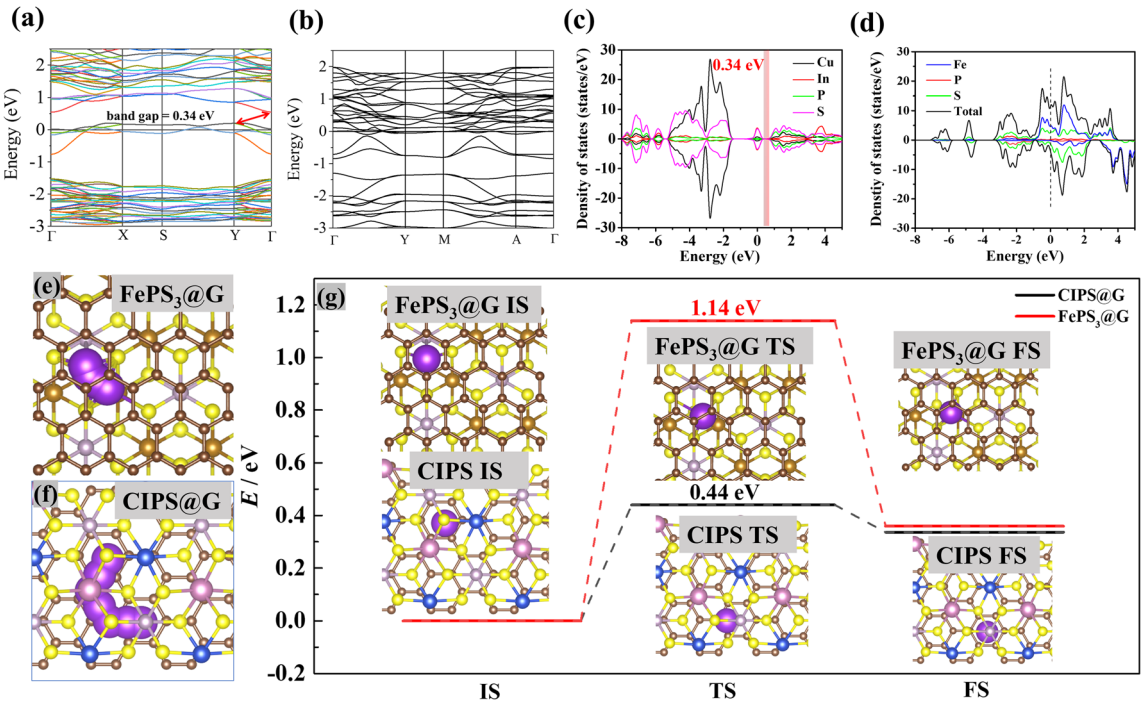

Fig. 7 Electronic band structure along the high-symmetry direction of (a) CIPS and (b) $FePS_3$. Projected density of states (PDOS) of (c) CIPS and (d) $FePS_3$. K migration path across (e) $FePS_3$@G and (f) CIPS@G. (g) Relative energy profiles of K migration across $FePS_3$@G and CIPS@G.

the DOS of $FePS_3$, P and S dominate the valence band, and Fe contributes significantly to the conduction band. To compare the performance of CIPS@G and $FePS_3$@G, we simulated the diffusion pathways of K^+ using different models to understand how the ferroelectric field affects their reaction kinetics and calculated their migration energies. Subsequently, we established the K^+ migration pathways in CIPS@G and $FePS_3$@G. Fig. 7e and f present a top-down view of the diffusion pathways for K^+ between $FePS_3$ and graphene, as well as between CIPS and graphene. We simplified the diffusion theory simulation of K^+ on the (001) crystal planes of $FePS_3$ and CIPS and summarized the diffusion energy barriers for different models (Fig. 7g). The diffusion energy barrier of the 2D room-temperature ferroelectric structure of CIPS@G is significantly lower than that of $FePS_3$@G, indicating that the 2D room-temperature ferroelectric structure of CIPS@G is more conducive to potassium diffusion. The K^+ diffusion energy barrier between CIPS and graphene is 0.44 eV, much lower than the 1.14 eV for anti-ferroelectric $FePS_3$ and graphene, suggesting that K^+ can diffuse more easily and rapidly in CIPS@G due to lower energy requirements. This implies that the 2D room-temperature ferroelectric structure of CIPS significantly influences the adsorption and migration of K^+ in energy storage processes, outperforming anti-ferroelectric $FePS_3$. This is not only related to the many rapid charge transfer nanochannels between 2D CIPS nanosheets and 2D graphene but also corresponds to the relative diffusion properties of anti-ferroelectric $FePS_3$@G and 2D room-temperature ferroelectric CIPS@G. The inherent dipole moment of CIPS@G, a characteristic of ferroelectric materials, generates a continuous polarizing electric field, facilitating rapid charge separation and transfer from the core of the material to the surface. Crucially, this ferroelectric field enhances ionic conductivity and K^+ diffusion, especially under high electric fields. Therefore, CIPS@G outperforms $FePS_3$@G in electrochemical performance, ensuring more efficient and reversible potassium storage. In conclusion, the results indicate that the unique ferroelectric properties of CIPS@G promote rapid electron/ion transport and excellent potassium storage.

We extended the application of CIPS@G as an anode in a potassium-ion full battery. The cathode, Prussian blue (PB), was chosen due to its high operating voltage and capability to withstand the high oxidation potential of K_2S_3. The XRD pattern of as-synthesized PB is shown in Fig. S22 (ESI†). PB's half-cell assembly shows a stable 56 mA h g^{-1} capacity (Fig. S23, ESI†). The CV curves of the CIPS@G//PB full cell significantly overlap (Fig. 8a), indicative of highly reversible chemical reactions, with

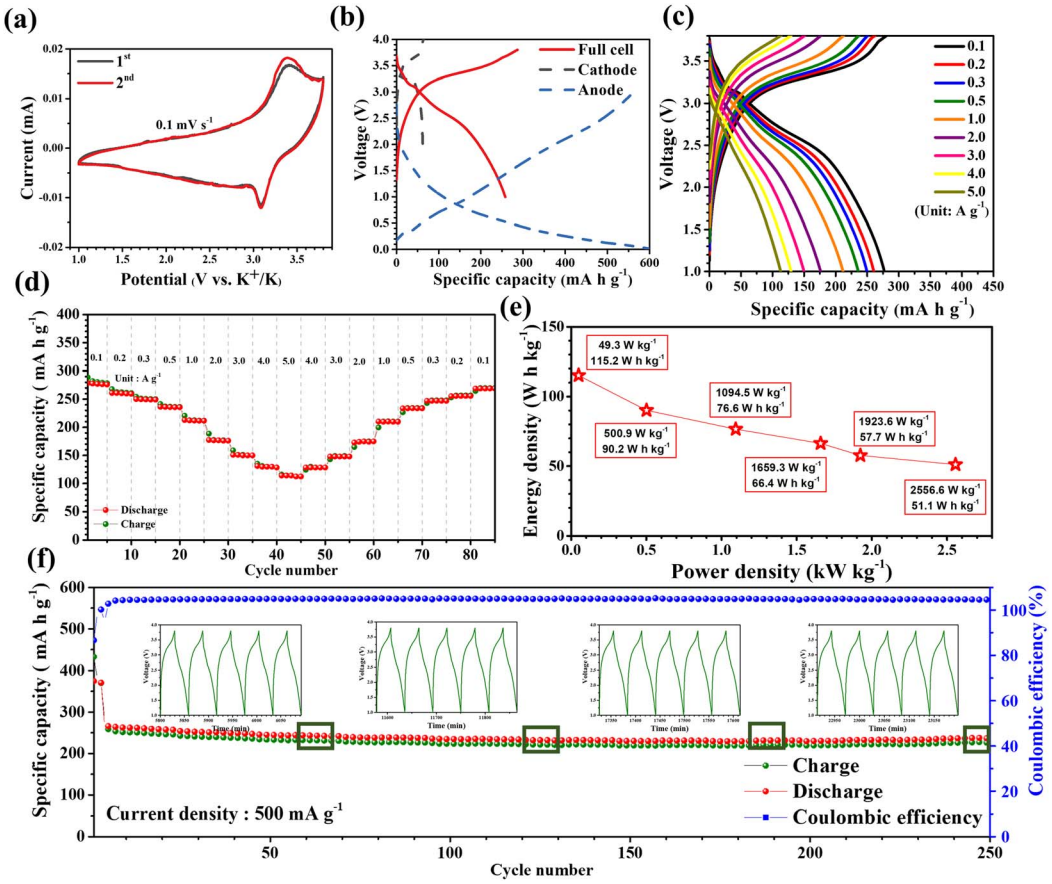

Fig. 8 Full cell of CIPS@G//PB. (a) CV curves of CIPS@G//PB in the 1st and 2nd cycles. (b) GCD curves of the PB and CIPS@G half-cell, and CIPS@G//PB full cell. (c and d) Rate capability at current densities ranging from 0.1 to 5.0 A g^{-1} and (e) the corresponding energy densities and power densities in the Ragone plot. (f) Long-term cycling performance of the CIPS@G//PB full cell at 500 mA g^{-1}.

notable redox peaks at 3.09 V and 3.38 V. In Fig. 8b, the GCD curves of the CIPS@G half-cell, the PB half-cell, and the CIPS@G//PB full-cell can be observed at a current density of 50 mA g^{-1}. The initial charge/discharge capacities of CIPS@G//PB are 286.95/257.93 mA h g^{-1}, respectively, consistent with the CV curve results. Notably, the anode's complete redox reaction in the conversion process delivers a significant specific capacity, leading to varied capacity contributions in either anodic or cathodic confinement. The rate performance of the CIPS@G//PB full cell, tested and illustrated in Fig. 8c and d, yields reversible capacities of 277, 261, 250, 236, 212, 177, 150, 130, and 114 mA h g^{-1} at respective current densities. A noticeable overpotential at a current density of 5.0 A g^{-1} leads to a slight plateau shift. Although there is a minor fluctuation in overpotential at high current densities, CIPS@G//PB demonstrates remarkable rate capability. The CIPS@G//PB full cell, with its high charge–discharge plateau, offers an energy density of 115.2 W h kg^{-1} and a power density of up to 2556.6 W kg^{-1}, based on the active materials of both electrodes (Fig. 8e), following standard battery calculations. During long-term testing at 300 mA g^{-1} (Fig. 8f), it sustains a 237 mA h g^{-1} capacity for over 400 cycles.

Moreover, we have constructed a potassium-ion hybrid capacitor (PIHC) asymmetric cell (CIPS@G//AC), comprising a CIPS@G anode and a commercial activated carbon (AC) cathode. This configuration underlines the merit of 2D materials in facilitating electron and K^+ transport, taking advantage of the quick diffusion and outstanding kinetic characteristics of K^+ in CIPS nanosheets. The FSI ions can traverse the electric double layer capacitance (EDLC) formed on the anode surface *via* adsorption and desorption in the electrolyte, resulting in high energy density.[67] The cell operates between 0.01 V and 3.8 V, delivering high energy/power densities. The CV curves of our assembled PIHCs display characteristic capacitive behavior (Fig. 9a), confirming no side reactions in the CIPS@G//AC hybrid capacitors within this voltage range. Fig. S24 (ESI†) and Fig. 9b show the CV curves of AC electrodes at 0.1 mV s^{-1} and those of CIPS@G//AC recorded at 1.0, 5.0, 10, 20, and 50 mV s^{-1}. High-rate CV curve analysis reveals no significant overpotential shifts, indicating pseudocapacitance predominance. Also, the linear GCD curve corresponding to hybrid capacitor behavior, as depicted in Fig. 9c, contributes to favorable rate performance. As illustrated in Fig. 9d, CIPS@G//AC capacitors deliver strong rate performance with energy densities of 112.17, 90.01, 74.01, 58.61, and 39.89 W h kg^{-1} at 50, 200, 500, 1000, and 2000 mA g^{-1}, respectively. Even when the current density reverts to 200 mA g^{-1}, a solid energy density of 84.53 W h kg^{-1} is maintained, showing excellent reversibility. Particularly, the

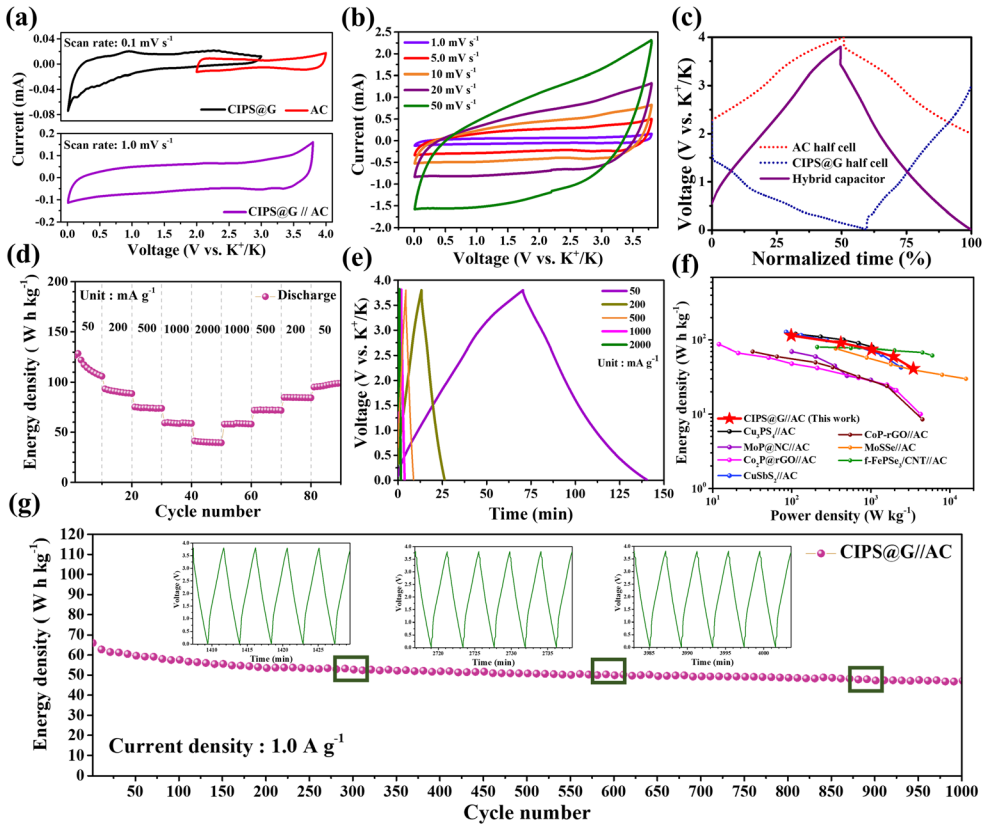

Fig. 9 Hybrid capacitor of CIPS@G//AC. (a) CV curves of the AC half-cell, CIPS@G half-cell and CIPS@G//AC PIHC. (b) CV curves and (c) normalized GCD curves of CIPS@G//AC at various scan rates. (d) Rate performance and (e) the corresponded normalized GCD curves at current densities from 50 to 2000 mA g^{-1}. (f) Ragone plot of CIPS@G//AC in comparison with reported PIHCs. (g) Long-term cycling performance of CIPS@G//AC at 1.0 A g^{-1}.

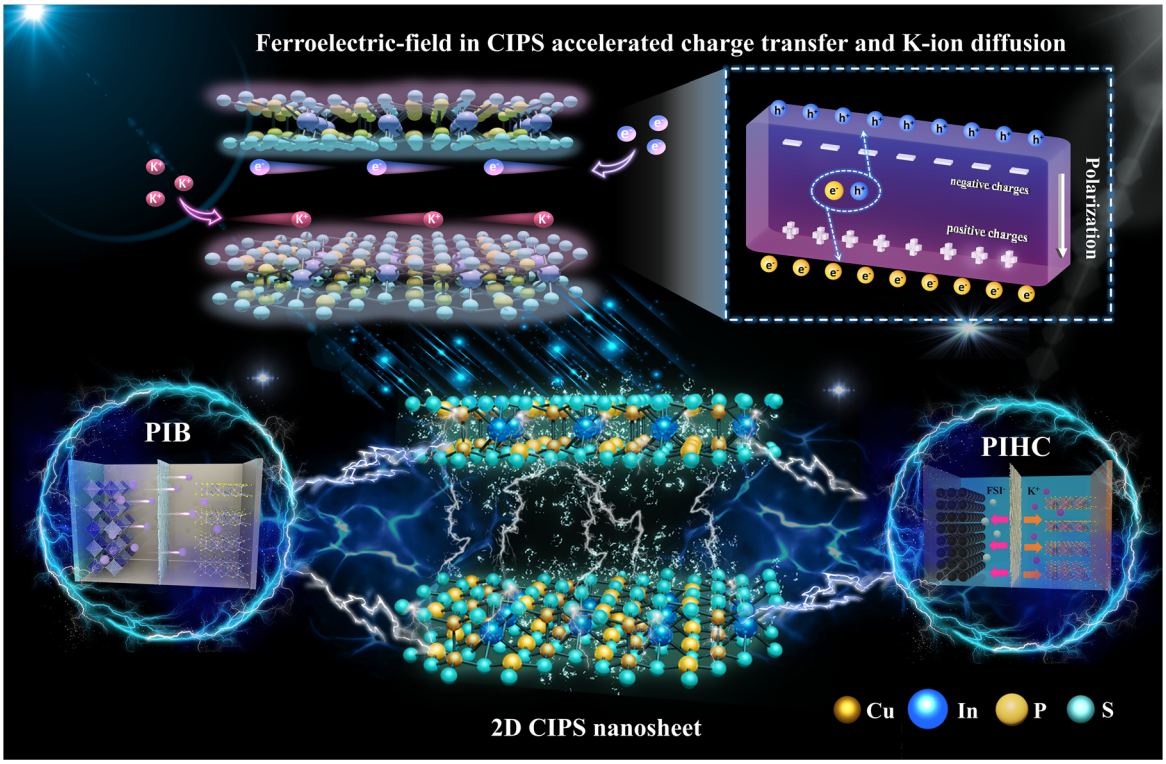

Fig. 10 Schematic diagram of the ferroelectric-field effect and applications of CIPS PIB anodes.

GCD curves for CIPS@G//AC at different current densities are shown in . At 50 mA g^{-1}, it sustains a high energy density of 112.17 W h kg^{-1}, significantly exceeding those of most other PIHCs. The Ragone diagram (Fig. 9f) featuring energy/power densities of sulfide and phosphide compounds attests to the new CIPS@G//AC PIHC capacitor's superiority over other materials such as Cu_3PS_4//AC,[68] MoP@NC//AC,[69] *etc*. The PIHC shows substantial long-term cycling performance, delivering 50 W h kg^{-1} energy density at 1.0 A g^{-1} (Fig. 9g) and maintaining 83.3% retention even after 1000 cycles. The enhanced performance of CIPS@G//AC can be attributed to the abundance of active sites in CIPS, which ensure efficient adsorption and a high capacity during the faradaic process.

Fig. 10 illustrates the specific manifestations of $CuInP_2S_6$ with ferroelectric properties in a PIB and PIHC. $CuInP_2S_6$ exhibits ferroelectric behavior at room temperature, driven by its spontaneous polarization characteristics, which enhance ion conductivity. Under high electric fields, there is an increase in charge at the electrode interface and the transport of K^+. The effectiveness of $CuInP_2S_6$ in both PIB and PIHC configurations has been demonstrated. In summary, the spontaneous polarization phenomenon generated by the unique ferroelectric crystal structure of $CuInP_2S_6$ enables rapid and stable potassium-ion migration within the material, establishing high-performance and long-life potassium-ion batteries. The ferroelectric effect of $CuInP_2S_6$ also makes significant contributions to potassium-ion storage, yielding superior capacitance compared to two-dimensional van der Waals materials lacking ferroelectric properties. This improvement addresses the shortcomings of traditional 2D materials in energy storage while further supporting the hypothesis that ferroelectric effects enhance electrochemical performance.

4 Conclusion

In conclusion, our study merges ferroelectric concepts with 2D materials, *i.e.*, CIPS, to advance K^+ storage. Analyzing CIPS across different temperatures highlighted the performance gains from ferroelectric field effects. The presence of the ferroelectric polarization field aids in charge and ion movement, with the nanochannels between CIPS and graphene further enhancing these kinetics. Thanks to its benefits, the CIPS@G anode for potassium-ion batteries boasts high reversible capacity, outstanding cycling stability, and rate capability, along with impressive coulombic efficiency and energy density in full cells and hybrid capacitors. This research pioneers the connection between the ferroelectric field effect and the energy storage potential of these materials. The combined effects of high-rate charge-transporting nanochannels between 2D CIPS nanosheets and graphene, along with CIPS's ferroelectric polarization, enhance electronic conductivity. This synergy aids K^+ diffusion, reduces CIPS aggregation, and manages volume changes, showing the potential of 2D materials in K^+ storage devices and broadening their use in energy storage systems. In general, the development of 2D ferroelectrics in the field of energy storage is in the early stages of exploration. With the improvement of ferroelectric electrode materials, the exploration of material properties and the understanding of the basic

principles of electrochemical behavior, two-dimensional ferroelectrics may become a competitive and attractive application choice for large-scale energy storage systems in the future.

Author contributions

Hsing-Yu Tuan carried out the conceptualization, methodology, and data curation, and drafted the final manuscript. Yi-Chun Yang handled the data curation. Po-Wen Chien was responsible for conceptualization, resource acquisition, and project supervision, and wrote the final manuscript. Yu-Bo Hung handled the review and editing of the final manuscript, as well as supplementing the experimental data.

Conflicts of interest

The authors declare that they have no known competing financial interests or personal relationships that could have appeared to influence the work reported in this paper.

Data availability

The datasets generated and/or analyzed during the current study are available from the corresponding author on reasonable request. ESI† is included with the article.

Acknowledgements

This work received financial support from the 2030 Cross-Generation Young Scholars Program by the Ministry of Science and Technology, Taiwan (NSTC 112-2628-E-007-010 and NSTC 112-2628-E-007-016). The authors thank Mr Yung-Sheng Chen (Instrumentation Center at NTHU) for spherical-aberration corrected field emission TEM analysis.

Notes and references

1 Y. Gao, W. Li, B. Ou, S. Zhang, H. Wang, J. Hu, F. Kang and D. Zhai, *Adv. Funct. Mater.*, 2023, **33**, 2305829.
2 S. Liu, L. Kang and S. C. Jun, *Adv. Mater.*, 2021, **33**, 2004689.
3 X. Yu, X. Ren, Z. Yuan, X. Hou, T. Yang and M. Wang, *Adv. Sci.*, 2023, **10**, 2205556.
4 K. Qin, K. Holguin, J. Huang, M. Mohammadiroudbari, F. Chen, Z. Yang, G.-L. Xu and C. Luo, *Adv. Sci.*, 2022, **9**, 2106116.
5 J. Liao, C. Chen, Q. Hu, Y. Du, Y. He, Y. Xu, Z. Zhang and X. Zhou, *Angew. Chem.*, 2021, **133**, 25779–25786.
6 L. Sun, G. Li, S. Zhang, S. Liu, J. Yuwono, J. Mao and Z. Guo, *Sci. China Chem.*, 2024, **67**, 4–12.
7 S. Li, Q. Zhang, H. Deng, S. Chen, X. Shen, Y. Yuan, Y. Cheng, J. Zhu and B. Lu, *Small Methods*, 2023, **7**, 2201554.
8 M. Shen, H. Ding, L. Fan, A. M. Rao, J. Zhou and B. Lu, *Adv. Funct. Mater.*, 2023, **33**, 2213362.
9 C. Ma, X. Tang, J. Jiang, Z. Ma, H. Li, H. Ben and X.-Z. Yuan, *Chem. Eng. J.*, 2023, **454**, 140116.
10 J. Zou, C. Fu, Y. Zhang, K. Fan, Y. Chen, C. Zhang, G. Zhang, H. Dai, Y. Cao, J. Ma and C. Wang, *Adv. Funct. Mater.*, 2023, **33**, 2303678.
11 H. Yang, J. Huang, S. Liu, Y. Chen, Z. Cen, C. Shi, Y. Lu and R. Fu, *Small*, 2023, **19**, 2302537.
12 Y.-F. Huang, Y.-C. Yang and H.-Y. Tuan, *Chem. Eng. J.*, 2023, **451**, 139013.
13 S. Liu, L. Kang, J. Hu, E. Jung, J. Henzie, A. Alowasheeir, J. Zhang, L. Miao, Y. Yamauchi and S. C. Jun, *Small*, 2022, **18**, 2104507.
14 E. K. Qian, A. K. Iyer, M. Cheng, K. M. Ryan, L. Jirousek, D. G. Chica, P. Krantz, Y.-S. Lee, V. Chandrasekhar, V. P. Dravid and M. G. Kanatzidis, *Chem. Mater.*, 2023, **35**, 3671–3685.
15 D. G. Chica, A. K. Iyer, M. Cheng, K. M. Ryan, P. Krantz, C. Laing, R. dos Reis, V. Chandrasekhar, V. P. Dravid and M. G. Kanatzidis, *Inorg. Chem.*, 2021, **60**, 3502–3513.
16 H.-Y. Zhong, X. Lu, Y. Zhong, Y. Zhao, X.-M. Liu, D.-H. Cheng, X.-Y. Huang, K.-Z. Du and X.-H. Wu, *Small*, 2022, **18**, 2104295.
17 Q. Yun, Y. Ge, B. Chen, L. Li, Q. Wa, H. Long and H. Zhang, *Adv. Funct. Mater.*, 2022, **32**, 2202319.
18 Y. Zhu, L. Peng, Z. Fang, C. Yan, X. Zhang and G. Yu, *Adv. Mater.*, 2018, **30**, 1706347.
19 Q. He, Z. Tang, M. Dai, H. Shan, H. Yang, Y. Zhang and X. Luo, *Nano Lett.*, 2023, **23**, 3098–3105.
20 Z. Zhong, S. Wu, X. Li, Z. Wang, Q. Yang, B. Huang, Y. Chen, X. Wang, T. Lin, H. Shen, X. Meng, M. Wang, W. Shi, J. Wang, J. Chu and H. Huang, *ACS Nano*, 2023, **17**, 12563–12572.
21 X. Mao, J. Fu, C. Chen, Y. Li, H. Liu, M. Gong and H. Zeng, *ACS Appl. Mater. Interfaces*, 2021, **13**, 24250–24257.
22 P. D. Taylor, S. A. Tawfik and M. J. S. Spencer, *Nanotechnology*, 2023, **34**, 065701.
23 B. Lin, A. Chaturvedi, J. Di, L. You, C. Lai, R. Duan, J. Zhou, B. Xu, Z. Chen, P. Song, J. Peng, B. Ma, H. Liu, P. Meng, G. Yang, H. Zhang, Z. Liu and F. Liu, *Nano Energy*, 2020, **76**, 104972.
24 S. Liu, L. Kang, J. Zhang, S. C. Jun and Y. Yamauchi, *ACS Energy Lett.*, 2021, **6**, 4127–4154.
25 W. Miao, Y. Zhang, H. Li, Z. Zhang, L. Li, Z. Yu and W. Zhang, *J. Mater. Chem. A*, 2019, **7**, 5504–5512.
26 P.-W. Chien, C.-B. Chang and H.-Y. Tuan, *Energy Storage Mater.*, 2023, 102853.
27 J. Wu, H.-Y. Chen, N. Yang, J. Cao, X. Yan, F. Liu, Q. Sun, X. Ling, J. Guo and H. Wang, *Nat. Electron.*, 2020, **3**, 466–472.
28 M. Si, A. K. Saha, P.-Y. Liao, S. Gao, S. M. Neumayer, J. Jian, J. Qin, N. Balke Wisinger, H. Wang, P. Maksymovych, W. Wu, S. K. Gupta and P. D. Ye, *ACS Nano*, 2019, **13**, 8760–8765.
29 S. Wang, N. Fan, Z. Zhou, Y. Hu, Q. Hui, Q. Li, J. Xue, Z. Zhou, Z. Feng, Q. Yan, Y. Weng, R. Tang, F. Zheng, R. Fan, B. Xu, L. Fang and L. You, *ACS Appl. Mater. Interfaces*, 2022, **14**, 40126–40135.
30 K.-C. Lin, M.-W. Lin, M.-N. Hsu, G. Yu-Chen, Y.-C. Chao, H.-Y. Tuan, C.-S. Chiang and Y.-C. Hu, *Theranostics*, 2018, **8**, 2477.

31 H.-J. Yang, C.-Y. Chen, F.-W. Yuan and H.-Y. Tuan, *J. Phys. Chem. C*, 2013, **117**, 21955–21964.
32 F. Parmigiani, G. Pacchioni, F. Illas and P. S. Bagus, *J. Electron Spectrosc. Relat. Phenom.*, 1992, **59**, 255–269.
33 C.-Y. Fan, X.-H. Zhang, Y.-H. Shi, H.-Y. Xu, J.-P. Zhang and X.-L. Wu, *J. Mater. Chem. A*, 2019, **7**, 1529–1538.
34 P. Yu, F. Wang, J. Meng, T. A. Shifa, M. G. Sendeku, J. Fang, S. Li, Z. Cheng, X. Lou and J. He, *CrystEngComm*, 2021, **23**, 591–598.
35 J. A. Brehm, S. M. Neumayer, L. Tao, A. O'Hara, M. Chyasnavichus, M. A. Susner, M. A. McGuire, S. V. Kalinin, S. Jesse, P. Ganesh, S. T. Pantelides, P. Maksymovych and N. Balke, *Nat. Mater.*, 2020, **19**, 43–48.
36 A. Belianinov, Q. He, A. Dziaugys, P. Maksymovych, E. Eliseev, A. Borisevich, A. Morozovska, J. Banys, Y. Vysochanskii and S. V. Kalinin, *Nano Lett.*, 2015, **15**, 3808–3814.
37 F. Liu, L. You, K. L. Seyler, X. Li, P. Yu, J. Lin, X. Wang, J. Zhou, H. Wang, H. He, S. T. Pantelides, W. Zhou, P. Sharma, X. Xu, P. M. Ajayan, J. Wang and Z. Liu, *Nat. Commun.*, 2016, **7**, 12357.
38 L. You, Y. Zhang, S. Zhou, A. Chaturvedi, S. A. Morris, F. Liu, L. Chang, D. Ichinose, H. Funakubo, W. Hu, T. Wu, Z. Liu, S. Dong and J. Wang, *Sci. Adv.*, 2019, **5**, eaav3780.
39 Q. Li, R. Deng, Y. Chen, J. Gong, P. Wang, Q. Zheng, Y. Huo, F. Xie, X. Wei, C. Yang and D. Lin, *Small*, 2023, **19**, 2303642.
40 W. Zhang, P. Cao, Z. Zhang, Y. Zhao, Y. Zhang, L. Li, K. Yang, X. Li and L. Gu, *Chem. Eng. J.*, 2019, **364**, 123–131.
41 W. Zhang, X. Yao, S. Zhou, X. Li, L. Li, Z. Yu and L. Gu, *Small*, 2018, **14**, 1800423.
42 F. Yuan, Z. Li, D. Zhang, Q. Wang, H. Wang, H. Sun, Q. Yu, W. Wang and B. Wang, *Adv. Sci.*, 2022, **9**, 2200683.
43 Q. Peng, S. Zhang, H. Yang, B. Sheng, R. Xu, Q. Wang and Y. Yu, *ACS Nano*, 2020, **14**, 6024–6033.
44 K. Share, A. P. Cohn, R. Carter, B. Rogers and C. L. Pint, *ACS Nano*, 2016, **10**, 9738–9744.
45 M. Huang, B. Xi, L. Mi, Z. Zhang, W. Chen, J. Feng and S. Xiong, *Small*, 2022, **18**, 2107819.
46 C.-Y. Tsai, C.-H. Chang, T.-L. Kao, K.-T. Chen and H.-Y. Tuan, *Chem. Eng. J.*, 2021, **417**, 128552.
47 T. X. Nguyen, C.-C. Tsai, J. Patra, O. Clemens, J.-K. Chang and J.-M. Ting, *Chem. Eng. J.*, 2022, **430**, 132658.
48 L. Hu, Y. An, L. Zhang, L. Mai, T. Ma, Q. An and Q. Wang, *J. Energy Storage*, 2023, **72**, 108520.
49 X. Jia, E. Zhang, X. Yu and B. Lu, *Energy Technol.*, 2020, **8**, 1900987.
50 G. Suo, S. Musab Ahmed, Y. Cheng, J. Zhang, Z. Li, X. Hou, Y. Yang, X. Ye, L. Feng, L. Zhang and Q. Yu, *J. Colloid Interface Sci.*, 2022, **608**, 275–283.
51 J. Wang, L. Fan, Z. Liu, S. Chen, Q. Zhang, L. Wang, H. Yang, X. Yu and B. Lu, *ACS Nano*, 2019, **13**, 3703–3713.
52 W. Zhang, J. Chen, Y. Liu, S. Liu, X. Li, K. Yang and L. Li, *J. Alloys Compd.*, 2020, **823**, 153631.
53 X. Chen, N. Cheng, L. Zhang, G. Xiang, Y.-L. Ding and Z. Liu, *J. Alloys Compd.*, 2021, **861**, 158458.
54 Y. Yang, J. Wang, S. Liu, W. Zhu, G. Ye, X. Yi and B. Lu, *Chem. Eng. J.*, 2022, **435**, 134746.
55 H. Zhang, Y. Cheng, J. Sun, W. Ye, C. Ke, M. Cai, H. Gao, P. Wei, Q. Zhang and M.-S. Wang, *Adv. Energy Mater.*, 2022, **12**, 2201259.
56 X.-B. Cheng, C. Yan, X.-Q. Zhang, H. Liu and Q. Zhang, *ACS Energy Lett.*, 2018, **3**, 1564–1570.
57 C. Choi, D. Ashby, Y. Rao, E. Anber, J. L. Hart, D. Butts, C. Wilson, E. Levin, M. Taheri, M. Ghazisaeidi, B. Dunn and V. Doan-Nguyen, *ACS Appl. Mater. Interfaces*, 2022, **14**, 3980–3990.
58 S. Liu, L. Kang, J. Henzie, J. Zhang, J. Ha, M. A. Amin, M. S. A. Hossain, S. C. Jun and Y. Yamauchi, *ACS Nano*, 2021, **15**, 18931–18973.
59 B. Sun, Q. Zhang, C. Zhang, W. Xu, J. Wang, G. Yuan, W. Lv, X. Li and N. Yang, *Adv. Energy Mater.*, 2021, **11**, 2100082.
60 Y. Zhang, P. Chen, Q. Wang, Q. Wang, K. Zhu, K. Ye, G. Wang, D. Cao, J. Yan and Q. Zhang, *Adv. Energy Mater.*, 2021, **11**, 2101712.
61 Y.-Y. Hsieh and H.-Y. Tuan, *Energy Storage Mater.*, 2022, **51**, 789–805.
62 W. Zhang, Z. Yue, Q. Wang, X. Zeng, C. Fu, Q. Li, X. Li, L. Fang and L. Li, *Chem. Eng. J.*, 2020, **380**, 122548.
63 S. Huang, C. Meng, M. Xiao, S. Ren, S. Wang, D. Han, Y. Li and Y. Meng, *Small*, 2018, **14**, 1704367.
64 S. Dong, D. Yu, J. Yang, L. Jiang, J. Wang, L. Cheng, Y. Zhou, H. Yue, H. Wang and L. Guo, *Adv. Mater.*, 2020, **32**, 1908027.
65 P. Liu, J. Han, K. Zhu, Z. Dong and L. Jiao, *Adv. Energy Mater.*, 2020, **10**, 2000741.
66 K.-T. Chen, S. Chong, L. Yuan, Y.-C. Yang and H.-Y. Tuan, *Energy Storage Mater.*, 2021, **39**, 239–249.
67 C.-H. Chang, K.-T. Chen, Y.-Y. Hsieh, C.-B. Chang and H.-Y. Tuan, *ACS Nano*, 2022, **16**, 1486–1501.
68 S.-F. Ho and H.-Y. Tuan, *Chem. Eng. J.*, 2023, **452**, 139199.
69 W. Zong, N. Chui, Z. Tian, Y. Li, C. Yang, D. Rao, W. Wang, J. Huang, J. Wang, F. Lai and T. Liu, *Adv. Sci.*, 2021, **8**, 2004142.

